Fabiana Richter, Carmala N. Garzione, Weiguo Liu, Xiaoke Qiang, Hong Chang, Feng Cheng, Xiangzhong Li, and Aradhna Tripati, 2022, Plio-Pleistocene cooling of the northeastern Tibetan Plateau due to global climate change and surface uplift: GSA Bulletin, https://doi.org/10.1130/B36302.1.

Supplemental Material

Supplemental Methods 1. Statistical zonation and division of the core into units and subunits

Supplemental Methods 2. NETP Soil thermal profile

Supplemental Note 1. Season of carbonate formation

Supplemental Note 2. The use of modern T-elevation gradients applied to the past

Supplemental Note 3. Tectonic and climatic events around 3.6 Ma in the NETP

Supplemental Note 4. Depths of pedogenic carbonate formation in northern East Asia and uncertainties

Supplemental Figure S1. Division of the core.

Supplemental Figure S2. Core pictures showing the locations from where clumped-isotope samples were collected.

Supplemental Figure S3. Annual soil temperature variation and soil-temperature profiles in the literature compared to our models.

Supplemental Figure S4. Relationship between air and ground temperatures

Supplemental Figure S5. Changes in modern T-elevation gradients according to variations in mean temperatures.

Supplemental Figure S6. Plots of Δ47 versus δ^{18}O‰ and δ^{13}C‰ versus δ^{18}O‰ from clumped-isotope analyses.

Supplemental Figure S7. Plio-Pleistocene MAATs and paleoelevation estimates for the Lake Qinghai Basin (LQB) compared to regional and global records (AMJJASO transfer functions).

Supplemental Figure S8. Plio-Pleistocene MAATs and paleoelevation estimates for the Lake Qinghai Basin (LQB) compared to regional and global records (AMJJASO-JJA transfer functions).

Supplemental Figure S9. Modeled (underground) soil temperatures at depths ranging from 40 to 100 cm. See Supplemental Note 3 for details.

Supplemental Figure S10. Results of tests of significance between mean MAATs in the 4 age groups. The figure shows two-sample z-tets and two-sample-one-tail t-tests to help decided whether there is significant difference between the mean MAAT values of groups 1 and 2, 2 and 3, 3 and 4.

Supplemental Figure S11. Results of tests of significance between mean MAATs in the oldest segment (groups 1 and 2) and mean MAATs in the youngest segment (groups 3 and 4) (i.e., before and after 3.6 Ma). The figure shows two-sample z-tests and two-sample-one-tail t-tests to help decide whether there is a significant difference in mean MAATs of groups 1+2 (4.85–3.7 Ma) and groups 3+4 (3.5–2.06 Ma).

Supplemental Figure S12. Mineral compositions of 20 samples from the Yilang core spanning 3.0–3.8 Ma and sand percentage spanning 2.0–5.1 Ma. a) Composition of all samples. b) Percentage of calcite, dolomite and quartz. c) Percentage of calcite and dolomite. d) 100% stacked bar plot showing the proportion of calcite, dolomite and quartz. e) 100% stacked bar plot showing the relative proportions of carbonatic minerals calcite and dolomite. f) Percentage of sand and gravel (>63 μm) in the core, SEM samples, and clumped isotope samples from 2.0 to 5.1 Ma.

Supplemental Data 1. Description of sediment core units and respective subunits based on sedimentary textures and structures. Mean oxygen and carbon isotopic composition of each unit and subunit.

Supplemental Data 2. Analytical results - oxygen and carbon carbonate isotopic composition. Interpreted environments are shown for each datapoint. Grain size and $CaCO_3$ content (%) also shown.

Supplemental Data 3. Summary of clumped-isotope analytical results, calculated MAATs and calculated elevations.

Supplemental Data 4. Air T, ground T and Relative humidity data measured in the NETP averaged during JJA, AMJJASO and annually. Data from 199 meteorological stations in the NETP region.

Supplemental Data 5. Lake T data for NH lakes above 20°N, based on the global compilation by Hren and Sheldon (2012).

Supplemental Data 6. Modeled underground Ts (soil Ts) for each station location during JJA and AMJJASO based on monthly air T and ground T from 199 weather stations in the NETP region.

Supplemental Data 7. Monthly air Ts and ground Ts ($z = 0$) from 199 weather stations in the NETP region are used to model NETP monthly and seasonal soil (underground) T profiles using soil physics principles.

Supplemental Data 8. Clumped isotope thermometry analytical results.

Supplemental Data 9. Monte Carlo simulations for each sample. In step 1, we use transfer functions to find MAATs corresponding to lake surface water Ts during AMJJASO. In step 2, we used calculated MAATs in step 1 to find corresponding elevations in the NETP region.

Supplemental Data 10. Monte Carlo simulations for each sample. In step 1, we use transfer functions to find MAATs corresponding to lake surface water Ts during JJA. In step 2, we used calculated MAATs in step 1 to find corresponding elevations in the NETP region.

Supplemental Data 11. Monte Carlo simulations for each sample. In step 1, we use transfer functions to find MAATs corresponding to soil Ts (50 cm depth) during AMJJASO. In step 2, we used calculated MAATs in step 1 to find corresponding elevations in the NETP region.

Supplemental Data 12. Monte Carlo simulations for each sample. In step 1, we use transfer functions to find MAATs corresponding to soil Ts (50 cm depth) during JJA. In step 2, we used calculated MAATs in step 1 to find corresponding elevations in the NETP region.

Supplemental Data 13. Calculation of cooling rates for the Lake Qinghai Basin and Weihe Basin (Wang et al., 2019). Calculation of average MAAT and elevation for the four main segments of the core.

Supplemental Data 14. Mineral components in samples spanning 3.0–3.8 Ma obtained from scanning electron microscope (SEM) analysis.

SUPPLEMENTAL METHODS

Supplemental Methods 1. Statistical zonation and division of the core into units and subunits

In order to evaluate if our sedimentology-based division was robust, we divided our data series into segments using a statistical zonation approach known as "local boundary hunting" (Davis, 2002). This method defines local boundaries associated with the steepest gradients in the series, i.e., higher rates of change in the dependent variable ($\delta^{18}O$, $\delta^{13}C$, grain size <4 μm %, grain size >40 μm %, grain size >63 μm %, CaCO3 content %) with respect to the independent variable (age). These gradients are calculated by examining how the dependent variable changes across a window 2h centered at each point. A comparison is made between the half window in advance of the data point {a: a+h} and the half window behind it {a: a-h}. In our case, the metric used to measure the difference between the two sides of the window for each point is the generalized distance (D^2)

$$D^2=\frac{(\mu_{-h}-\mu_{+h})^2}{\sigma^2{}_{-h}+\sigma^2{}_{+h}}$$

where μ is the arithmetic mean of the dependent variable, σ is the variance of the dependent variable and the subscripts indicate the halves of the window around each point. Given the resolution of our data set and after trial calculations, we chose a window h = 10 that we evaluated as appropriated not to create too much or too few segments. Supplemental Figure 1 shows dependent variable values and respective calculated D^2 values plotted versus age. We combined and plotted peaks in D^2 values obtained from all dependent variables versus age, interpreted to represent significant changes in grain size and/or stable isotope geochemistry. We compared these boundaries to the boundaries we have set based on core sedimentary textures and structures. We show that all of these sedimentology-based boundaries have a correspondent boundary found via the "local boundary hunting" method. However, not all boundaries found by the "local boundary method" have a correspondent sedimentology-based boundary. This suggests that all changes in depositional environments we have described are marked by geochemical and/or grain size changes in the record, yet some of these features cannot be determined visually.

Supplemental Methods 2. NETP Soil thermal profile

▪ Thermal regime of soil profiles

A soil T profile is built from a set of T values that are measured or modeled at the ground surface (z = 0 cm) and at different depths underground (z>0 cm) over the year. The simplest mathematical representation of a soil thermal regime assumes all depths in the soil have temperatures oscillating as a pure harmonic (sinusoidal) function of time around an average value (Hillel, 1982; Supplemental Fig. 3a). The underground annual T oscillates with the same frequency as the ground T, but, with depth, the wave amplitude decreases and the phase lag increases (Williams and Smith, 1989). The underground temperature (UT) at any depth (z) can be represented as a sine function of time (t):

$$UT(z,t) = MAGT + \frac{A_{ground}}{e^{z(\omega/2D)^{1/2}}} \sin\left[\omega t - z\left(\frac{\omega}{2D}\right)^{1/2}\right] \#(1)$$

where $MAGT$ is the mean annual ground (soil) temperature, assuming that the average soil temperature over the year is the same for all depths, i.e., soil temperatures vary differently at different depths around the same average (Supplemental Fig. 3a). A_{ground} is the amplitude of temperatures at the ground surface (z = 0 cm), i.e., the range from maximum, or from minimum temperature, to the annual average soil temperature at z = 0 (Hillel, 1982). The variable ω is the radial frequency (in radians), which equals 2π times the actual frequency. This is given by

$$\omega = \frac{2\pi}{P} \#(2)$$

where P is the period. In the case of annual variation, represented in seconds, $P = 365 \times 24 \times 60 \times 60 = 51536000\ sec$. The time t is the time (in seconds) of the year. This model assumes that the starting time (t = 0) occurs in Spring on the date in which the ground (surface) temperature wave passes through its mean annual value. The soil thermal diffusivity D is the ratio of the soil thermal conductivity (κ) to the soil volumetric heat capacity (C_v).

It is useful to introduce the concept of damping depth (d), implicit in Equation (1). Damping depth is a characteristic depth at which the temperature amplitude equals $1/e$ ($1/2.718 = 0.37$) of the amplitude at the soil surface (A_{ground}). The damping depth is related to the thermal properties of the soil and the frequency of temperature fluctuation (Hillel, 1982):

$$d = (2D/\omega)^{1/2} \#(3)$$

Therefore, we re-write Equation (1) as

$$UT(z,t) = MAGT + \frac{A_{ground}}{e^{z/d}} \sin(\omega t - z/d)\ \#(4)$$

In Equation (4), as well as in (1), the term $\frac{A_{ground}}{e^{z/d}}$ represents the amplitude at a depth z (A_z) and the term ($-z/d$) is a phase lag ($\phi(z)$), a time delay of the temperature peak with depth (Hillel, 1982).

Supplemental Figure 3.a illustrates how T oscillates in unfrozen soil over the year, which can be modeled using Equation (1). Underground T oscillations at different depths have the same frequency as the ground T oscillation, but T amplitude diminishes and phase lag increases with depth (Williams and Smith, 1989). Applying Equation (1), we are able to obtain mean seasonal Ts at each soil depth and generate a soil T profile as it varies from season to season (Supplemental Figure 3.b).

▪ **Thermal regime of NETP soil profiles**

Using a data set from meteorological stations on the Northeastern Tibetan Plateau (NETP) region and Equation (1), we modeled ground and underground temperature oscillations in the NETP over one year. Our data set was obtained from 199 meteorological stations whose locations are shown in Figure 1. These data were downloaded from the China Meteorological Data Sharing Service System (http://cdc.cma.gov.cn). At each station, the data set consists of monthly air and ground temperature measurements averaged over the period 1981–2010. These measurements followed "Specifications for surface meteorological observation" in China: air temperatures were measured at 1.5 m (z = -150 cm) off the ground; ground surface temperatures were measured at 0 cm depth at the soil surface with no vegetation. From this data set, we calculated mean monthly air Ts (MMATmeas), mean monthly ground Ts (MMGTmeas), mean annual air Ts (MAATmeas) and mean annual ground Ts (MAGTmeas), shown in Supplemental Data 7.

Using Equation (1), we modeled mean monthly ground T ($MMGT_{model}$) and mean monthly undergound T ($MMUT_{model}$) in the NETP. These temperatures change as a sinusoidal function of time (t), whose amplitude and phase lag will be controlled by the depth in question. Supplemental Figure 3c shows that $MMGT_{meas}$ are closely reproduced by our $MMGT_{model}$. Table 1 shows the values calculated for each month at 0 cm, 20 cm and 50 cm depth, which were used in Supplemental Figure 3c. Model assumptions are the following. To determine thermal diffusivity D, we assume $\kappa = 0.0007\ cal \times cm^{-1} \times sec^{-1} \times °C^{-1}$ and $C_v = 0.3\ cal \times cm^{-3} \times °C^{-1}$, following Quade et al. (2013). To determine A_{ground}, we use the average amplitude between the warmest and coldest monthly averages and $MAGT_{meas}$. We refer to this as $A_{ground,model}$, which equals half of the range between the warmest monthly average ground T (mean ground temperature in July, $MMGT_{Jul,meas}$) and the coldest monthly average ground T ($MMGT_{Jan,meas}$, mean ground temperature in January):

$$A_{groundmodel} = (MMGT_{Jul,meas} - MMGT_{Jan,meas})/2 \quad \#(5)$$

Finally, the model assumes the year starts (t = 0) at the beginning of April 1st, when model mean ground T in April ($MMGT_{Apr,model}$) is equal to $MAGT_{meas}$. Because actual $MMGT_{Apr,meas}$ is different from $MAGT_{meas}$, this approach yields a more significant difference between measured and model temperatures in April than in other months, but it yields the smallest difference between measured and model temperatures overall, particularly over the warmest half of the year (Supplemental Data 7). Supplemental Figure 3c shows the decrease in temperature amplitude and time lag with depth at z = 20 and z = 50 cm. For instance, at z = 0 and z = 20 cm, soil is warmest over the June, July and August period, as are air temperatures. However, at z = 50, soil is warmest over the July, August and September period.

Using calculated values at different depths (z from 0 to 250 cm) on each month, we were able to construct a soil T profile as it varies over one year. Supplemental Figure 3d shows calculated T profiles for all months as well as profiles for average temperatures over the June-August (JJA) period and for average temperatures over the April-October period (AMJJASO). For comparison with model temperatures at z = 0, we plotted $MMGT_{meas}$, also shown in Supplemental Data 7.

Table 1. Parameters from model used to plot Supplemental Figure 3c.

Beginning	Seconds/month	Days/month	Seconds since t = 0	MMATmeas (z = -150)	MMGTmeas (z = 0 cm)	Ground T amplitude (Asurfmodel)	Air T amplitude (Aairmodel)	MMUTmodel (z = 0 cm)	MMUTmodel (z = 20 cm)	MMUTmodel (z = 50 cm)
April	0	-	0	8.55	12.53	-	-	9.96	8.16	6.33
May	2678400	31	2678400	13.69	18.71	-	-	17.93	15.35	12.28
June	2592000	30	5270400	17.52	22.87	-	-	23.56	20.90	17.44
July	2678400	31	7948800	19.64	24.78	-	-	25.64	23.62	20.72
August	2678400	31	10627200	18.31	22.72	-	-	23.35	22.55	21.00
September	2592000	30	13219200	13.64	16.79	-	-	17.58	18.16	18.34
October	2678400	31	15897600	7.22	9.25	-	-	9.55	11.40	13.31
November	2592000	30	18489600	0.08	0.97	-	-	1.86	4.45	7.54
December	2678400	31	21168000	-5.63	-5.41	-	-	-3.84	-1.20	2.25
January	2678400	31	23846400	-7.15	-6.59	-	-	-5.71	-3.75	-0.89
February	2419200	28	26265600	-3.48	-1.90	-	-	-3.65	-2.77	-1.14
March	2678400	31	28944000	2.09	4.76	-	-	2.21	1.66	1.51
April	2592000	30	31536000	8.55	12.53	-	-	9.96	8.16	6.33
Year	31536000	365	31536000	7.04	9.96	15.68	13.39	-	-	-

▪ Relationship between soil T and air T in the NETP region

In this study, we are using the Δ_{47}T of PC samples to calculate corresponding air temperatures above soils in which they formed. This can be achieved by using soil physics to build a model representing air and underground (soil) temperature change as a function of changing time and ground depth. Supplemental Figure 3 resulted from application of soil physics to model ground subsurface temperature change over time and with depth using temperature information averaged from 199 stations in the NETP (Fig. 1a). Taking the same approach, we modeled such relationships for each of these 199 stations in order to understand the relationship between soil and air temperatures at each location in the NETP region. We applied the model for each station to find modeled ground (z = 0 cm) soil (z = 50 cm) T, where 50 cm is interpreted to represent an average depth of carbonate formation. Based on MAATs and modeled soil (z = 50) T at each weather station location, we built transfer functions between MAAT and soil T during the periods of JJA ($MAAT_{JJA,soil}$) and AMJJASO ($MAAT_{AMJJASO,soil}$) (Fig. 6.a; Supplemental Data 6):

$$MAAT_{AMJJASO,soil} = 0.97(\Delta_{47}\mathrm{T}) - 8.08$$

Where the s.e. of the intercept is 0.29 and of the slope is 0.02; R^2 is 0.94; with a 95% confidence level.

$$MAAT_{JJA,soil} = 0.87(\Delta_{47}\mathrm{T}) - 10.02$$

Where the s.e. of the intercept is 0.49 and of the slope is 0.02; R^2 is 0.87; with a 95% confidence level.

Supplemental Figure 6 shows how MAATs relate to measured ground T (z = 0), to model ground T (z = 0), and to underground Ts (z = 50) during JJA and AMJJASO periods. Linear regression lines from MAATs versus measured ground T (z = 0) and MAATs versus model ground T (z = 0) relationships are very similar, particularly for the AMJJASO period. This indicates modeled ground values are a reasonable representation of measured ground values and its relationship with air Ts. We assume the same is true for the relationships between MAATs and modeled soil (z = 50) T, which we use in this study to represent the relationship between MAATs and Δ_{47}T of carbonate formation.

SUPPLEMENTAL NOTES

Supplemental Note 1. Season of carbonate formation

One step in this study involves building transfer functions that relate measured T of carbonate formation (Δ_{47}T) in paleolacustrine and paleosol settings to corresponding MAATs. We do this by using modern relationships between lake surface Ts and MAATs and between soil Ts and MAATs. Because most carbonate precipitation occurs seasonally in both settings, we need to understand the timing of carbonate formation in order to build robust transfer functions between MAATs and seasonal temperatures of carbonate formation. In addition, we need to understand whether these relationships are applicable to paleoenvironmental settings in the NETP during the Plio-Pleistocene.

In lacustrine settings, including Lake Kusai (4480 m.a.s.l.) in the northern Qinghai-Tibetan Plateau (Liu et al., 2014), micrite precipitated during whiting events form carbonate-rich varve layers whose thicknesses have been shown to positively correlate with summer Ts (e.g., Moore et al., 2001). This pattern holds in low-elevation Lake Mead (375 a.s.l.), located in the arid southwest of the Colorado Plateau in the USA, where modern carbonate growth $\Delta_{47}T_s$ corresponds to measured spring to summer water T records (Huntington et al., 2010). Likewise, carbonates in paleolacustrine settings on the Colorado Plateau, at relatively high elevations since the Miocene, have been interpreted to record warm season Δ_{47} paleotemperatures (Huntington et al., 2010). In pedogenic settings, carbonate tends to accumulate during soil drying when evapotranspiration exceeds precipitation, which, in mid-latitude arid settings, occurs during the warmest and/or driest months of the year (e.g., Breecker et al., 2009; Quade et al., 2013). For instance, at locations below 3200 m.a.s.l. in the arid western Andes (Chile), soil moisture is affected by the largest precipitation events in the wet season and, after prolonged periods of high temperature, deeper soils (>40 cm) dry and pedogenic carbonate forms, thus recording warm season $\Delta_{47}T_s$ (Burgener et al., 2016). We infer that, in northern East Asia, pedogenic carbonate formation occurs in the late Summer, coinciding with the time of the year where monsoonal rainfall starts to decrease and soils at depth are warmest, based on our modeled soil thermal profile (Supplemental Fig. 3). As there is evidence for East Asian monsoon conditions since at least the Miocene (Guo et al., 2002), we assume similar carbonate precipitation patterns in this Plio-Pleistocene record. Although we infer carbonates were mainly forming during the JJA period during Plio-Pleistocene, we have considered two alternate scenarios where carbonate precipitates: during the April-May-June-July-August-September-October (AMJJASO) growing season (Supplemental Fig. 7); or during AMJJASO before 3.7 Ma and during JJA afterwards

(Supplemental Fig. 8). We consider the second scenario because most recent studies suggest that the EASM weakened after ~4.0 Ma while warm-season precipitation decreased from 427 to 1197 mm (11–4.2 Ma) to 417–540 mm (4.2–2.6 Ma) in the CLP (Wang et al., 2019). This may have caused shortening of the growing season, although it is unclear whether that shortening is accurately represented by a shift from AMJJASO to JJA period that have affected the Lake Qinghai Basin from 3.72 to 3.58 Ma (see "Paleoenvironmental conditions based on the stable isotopic composition of carbonates and water" section). Given all the above, and that we cannot presently ascribe an exact time for this hypothetical transition or its effects in the timing of carbonate precipitation, we infer that using soil/lake JJA Ts in transfer functions yields the most representative estimates of MAATs.

Supplemental Note 2. The use of modern T-elevation gradients applied to the past

This study provides estimates of Plio-Pleistocene paleoelevations in the Lake Qinghai Basin from calculated past MAATs based on Δ_{47}T of carbonates. To estimate paleoelevations, we used a modern MAAT-elevation gradient (Fig. 6c) calculated from 199 weather stations in the NETP region (Fig. 1a). This assumes that even if the NETP had higher MAATs and/or was more humid in the past, T-elevation gradients then and now would be similar. Here we examine the effects of varying MAATs and mean relative humidity in T-elevation gradients. Note that we use the term "increasing" gradient to indicate an increase in the rates of cooling with respect to elevation.

With respect to changes in MAATs, modern data on the NETP (Fig. 6c; Supplemental Data 4) suggest that T-elevation gradients do not change significantly throughout the year, even with very different monthly and seasonal mean Ts. Supplemental Figure 5 shows that pattern. For instance, mean AMJJASO Ts are ~5 °C warmer than modern MAATs, but show T-elevation gradients (−4.8 °C/km) that are only slightly higher than MAAT-elevation gradients (−4.5 °C/km). The same pattern of T-elevation gradient similarity was observed for modern temperatures on the Colorado Plateau, where average monthly Ts vary by more than 20 °C yet monthly T-elevation gradients vary by less than 1 °C throughout the year (Huntington et al., 2010). This supports many studies that have used modern T-elevation gradients in paleoelevation reconstructions over periods that also experienced climate change. For instance, Gregory and McIntosh (1996) have applied modern T-elevation gradients to reconstruct paleoelevations in the southwestern United States dating back to the Eocene. Huntington et al. (2010) have used modern T-elevation gradients to reconstruct paleoelevations of the southern Colorado Plateau based on Miocene lacustrine records. They assumed such gradients were applicable because: 1) modern monthly gradients for the Colorado Plateau were very similar even with large variations in mean monthly values, as mentioned above; and 2) Miocene paleoenvironmental conditions were arid and semi-arid, similar to their modern study region. Their study found that temperatures have decreased since the Miocene, but paleoelevations remained similar to modern since ~6 Ma. In this study, we are considering the possibility that early Pliocene paleoenvironmental conditions on the NETP were not only warmer but also wetter. Our modern T data from weather stations indicate that temperature increase would slightly increase T-elevation gradients (Supplemental Fig. 5). This pattern is consistent with T-elevation gradients in mid-latitude continental interiors globally (Meyer, 1992). Relative humidity seems to have the opposite effect on these gradients. Today the lowest gradients (−3 to −4 °C/km) are found in the tropical humid regions on the planet (Meyer, 1986; Schneider, 2007). This suggests that, in such

regions, high relative humidity may lead to more condensation of water into clouds, which releases latent heat as sensible heat into the system. This would decrease the rate of cooling of humid air with respect to elevation.

The above mentioned suggests that opposite effects on T-elevation gradients are found by decreasing MAATs (decreases gradient) and decreasing relative humidity (increases gradient). Such changes may have occurred in our study area, based on our results and paleoenvironmental data compilation, but we infer they would have a negligible effect on the difference between modern and past T-elevation gradients because of two reasons. First, only high differences of MAATs and humidity are able to alter T-elevation gradients significantly, which is not observed in our record. For instance, if MAATs were ~6 °C warmer in the early Pliocene in our study area, this would increase gradients in about ~-0.4 °C/km based on modern climate data (Supplemental Fig. 5). In addition, data compilation suggests that paleoenvironmental conditions were relatively more humid in early Pliocene than in the Pleistocene, but these were still semi-arid environments. Second, the effects of increased MAATs and increased relative humidity in the early Pliocene on T-elevation gradients would partially cancel each other. Therefore, we infer that we can reasonably use modern T-elevation gradients on the NETP region for paleoelevation reconstructions in the Plio-Pleistocene.

Supplemental Note 3. Tectonic and climatic events around 3.6 Ma in the NETP

Compilation of data from previous studies that report tectonic and/or climatic events recorded in basins on the margins of the northeastern Tibetan Plateau in the Pliocene. These events, summarized in the Table below, include: growth strata in the Guide Basin (Li et al., 2014), in the Juxi Basin (Hexi Corridor; Fang et al., 2005; Li et al., 2014; Zheng et al. 2017, Chen et al., 2006) in the northeastern Qaidam Basin (Fang et al., 2007; Li et al., 2014); unconformity onset in the Juxi Basin (Hexi Corridor; Fang et al., 2005; Li et al., 2014; Zheng et al. 2017; Chen et al., 2006), in the Linxia Basin (Li et al., 1996), in the Lanzhou Basin (Sun et al., 2011), in the Tianshui Basin (Li et al., 2014) and in the western Qaidam Basin (Zhang et al., 2013); basin rotation in the Jiuquan Basin (Hexi Corridor; Yan et al., 2013) and in the Chaka Basin (Zhang et al., 2012); thrusting in the Guide Basin (Fang et al., 2005) and in the Hei Shan (Liu, 2017) and folding in the Juxi Basin (Hexi Corridor; Laojunmiao; Fang et al., 2005; Zheng et al., 2017) and in the Linxia Basin (Fang et al., 2003).

LOCATION	TIME FRAME	RECORD	REFERENCE
Guide Basin *(Ganjia and Amigang sections)*	3.6–2.6 Ma	*Coarsening:* deposition of boulder conglomerates of the Ganjia Fm. Clasts sourced from the Laji Shan.	Fang et al. (2005)
	3.2 Ma	*Sedimentation rates*: increased abruptly from ~0.2 mm/yr to 0.5 mm/yr in Ganjia Fm.	Fang et al. (2005)
	~3.6 Ma	*Thrusting*: south-verging thrust faulting (F4 and F5 faults) led to significant shortening of the Guide Basin.	Fang et al. (2005)
	3.6–1.8 Ma	Growth strata: onset at the Ganjia Fm., up to Amigang Fm.	Li et al. (2014)
Juxi Basin (*Laojunmiao anticline)*	4.9 to ~3.6 Ma	*Syntectonic unconformity:* at the base of Yumen Conglomerate.	Fang et al. (2005); Li et al. (2014); Zheng et al. (2017)
	~3.6 Ma	*Folding:* formation of Laojunmiao anticline.	Fang et al. (2005); Zheng et al. (2017)
	3.66—0.93 Ma	*Coarsening:* Deposition of Yumen Conglomerate (subangular to subrounded poorly sorted gravels).	Fang et al. (2005)
	~3.66 Ma	*Growth strata:* appearance near the base of Yumen Conglomerate.	Fang et al. (2005); Li et al. (2014); Zheng et al. (2017)
	~3.66 Ma	*Sedimentation rates:* Increased from average of 0.27 mm/yr before the unconformity at the base of Yumen Conglomerate to ~0.35 - 0.6 mm/yr at ~3.66 Ma.	Fang et al. (2005)
	3.1–2.6 Ma	*Unconformity*: First angular unconformity developed	Chen et al. (2006)
	3.0 Ma	*Growth Strata:* initiation at 3.0 Ma	Chen et al. (2006)
Juxi Basin (*Caogou section)*	~5–2.8 Ma	*Coarsening:* Deposition of Yumen Conglomerate (subangular to subrounded poorly sorted gravels). Clasts sourced from the North Qilian Shan.	Wang et al. (2016)
Juxi Basin *(Yumu Shan)*	3.7 ± 0.9 Ma	Growth of the Yumu Shan started.	Palumbo et al. (2009)
Juxi Basin *(Jiuquan Basin)*	after 4.0 Ma	*Basin rotation:* slight clockwise rotation of the basin based on magnetic declinations of paleomagnetic samples.	Yan et al. (2013)
Juxi Basin *(Juidong Basin)*	4.1–3.0 Ma	*Sedimentary facies change and coarsening*: At 4.1 Ma, sedimentar facies changed from delta to meandering river and at 3.6 conglomerates in the Laojunmiao and Yumushan sections were deposited. At 3.0 Ma, the meandering river regime changed to a braided river regime without substantial increase in sediment accumulation rate. This indicates continuous relief growth of the Qilian Shan from 3.6 to 3.0 Ma. At 3.0 Ma, the thrust system of the Qilian Shan propagated into the basin along a southward dipping décollement.	Hu et al. (2019)
	after 4.5 Ma	*Coarsening:* deposition of Yumen Conglomerate, Wenshushan anticline.	Zhao et al. (2001)
Hei Shan	3.8–2.8 Ma	Thrust Fault onset	Liu (2017)
Linxia Basin (*Wangjiashan (WJS) and central Maogou sections)*	6–3.6 Ma	*Folding:* tilting and folding of the strata in the Yingchuangou anticline.	Fang et al. (2003)
	4.5–3.6 Ma	*Unconformity:* between the Jishi Fm. and the underlying Hewangjia Fm.	Li et al. (1996)
	~3.6 Ma	*Coarsening:* Deposition of boulder conglomerates of the Jishi Fm. in the proximal part of the Linxia Basin. Clasts sourced from the Tibetan Plateau, southwest from Linxia Basin.	Li et al. (1996); Fang et al. (2003)
Lanzhou Basin (*Nanshan section)*	~3.5 Ma	*Coarsening:* deposition of Wuquan gravel layer (~3.5 Ma) over Terciary Red Clay.	Sun et al. (2011)
	3.5–1.8 Ma	*Unconformity:* located between Wuquan gravel layer and overlying Quaternary Loess (>3.5 Ma).	Sun et al. (2011)

Northeastern Qaidam Basin *(Huaitoutala section)*	3.6 Ma	*Sedimentation rates:* sharp increase within the Shizigou Formation (8.1–2.5 Ma).	Fang et al. (2007)
	3.6–1.8 Ma	*Growth strata*: narrow interval occurred synchronously with increase in sedimentation rates.	Fang et al. (2007); Li et al. (2014)
	>2.5 Ma	*Coarsening:* deposition of the conglomeratic Qihequan Formation.	Fang et al. (2007)
Chaka Basin	4.6–4 Ma	*Coarsening:* Deposition of a conglomerate group (Nc). Clasts are sourced mainly from Qinghai Nan Shan.	Zhang et al. (2012)
	4–3 Ma	*Basin rotation:* Local clockwise rotation of the Chaka Basin.	Zhang et al. (2012)
Tianshui Basin	~3.7–3.4 Ma	*Unconformity*.	Li et al. (2014)
Western Qaidam Basin *(Qigequan anticline against the southern edge of the Altyn Tagh)*	3.6 Ma	*Sedimentation rate:* increase of the accumulation rate at 3.6 Ma is accompanied by the appearance of conglomerate, indicative of a synchronous folding of the Qigequan anticline.	Zhang et al. (2013)
	2.5 Ma	*Unconformity:* appearance of an unconformity at 2.5 Ma, synchronous with the occurrence of a change of stratum dipping from 45° to 23°.	Zhang et al. (2013)

Supplemental Note 4. Depths of pedogenic carbonate formation in northern East Asia and uncertainties

Pedogenic carbonates (PC) are nodules, coatings, and diffuse carbonate that form in soils with a net water deficit during the warmest and/or driest months of the year in mid-latitude arid settings (Breecker et al., 2009). The upper and maximum depths of pedogenic carbonate accumulation in soil profiles, known as Bk horizons, are given by a complex combination of mean annual precipitation (MAP), seasonally controlled soil temperature and water balance, the initial carbonate content in parent material, and soil physics properties (Zamanian et al., 2016). As MAP is only one of the factors affecting depth of carbonate formation, the relationship between depth to Bk horizon and MAP based on a compiled global data set (n = 1542; Zamanian et al., 2016) indicates there is a low correlation between them ($R^2 = 0.34$). However, the same data set showed that depths to Bk horizons are commonly <100 cm deep when MAP is 100–800 mm. We can use this relationship to estimate a range of depths in which carbonate formation would likely occur in northern East Asia. Wang et al. (2019) estimated Mio-Pleistocene MAP and mean annual temperature (MAT) using a sedimentary record of phytoliths (plant silica) from the Weihe Basin, located east of the NETP: 800–1673 mm and 11–15.3 °C from 11 to 4.2 Ma; 812–900 mm and 9.7–11 °C from 4.2 to 2.6 Ma; and 441–540 mm and 3.3–11 °C from 2.6 to 0 Ma. Assuming these MAP estimates from a low-elevation region that is more strongly affected by the East Asian Summer monsoon would represent the maximum values possible for the high-elevation NETP, it is inferred that, in the NETP, MAP was lower than ~800 mm from 11 to 2.6 Ma and lower than 441 mm from 2.6 to 0 Ma. This agrees with pre-industrial MAP in the NETP ranging from 100 to 300 mm (Yang et al., 2014). Based on the global data set (Zamanian et al., 2016), these MAP values would be consistent with carbonate forming at depths <100 cm in the NETP during the Plio-Pleistocene.

Burgener et al. (2016) examined the relationship between air temperatures, elevation and soil PC Δ_{47}T in the western Andes (Chile), an arid region that experiences a winter wet season. They found that below 3200 m, PC forming at depths <40 cm can be affected by short-term temperature change following precipitation events (Burgener et al., 2016) and soil logger measurements show soil Ts fluctuate significantly on a daily basis at depths <30 cm (Quade et al., 2013). In other words, PC forming at depths lower than 30–40 cm are not good records of seasonal temperatures. On the other hand, PC formed at depths >40 cm will likely form during the warmest and driest season, and thus PC Δ_{47}Ts would represent (warm) seasonal soil

temperature records. At depths >40 cm in the western Andes (Burgener et al., 2016), soil moisture is only affected by the largest precipitation events in the wet season, which will modulate the timing of PC formation. In the following warm (dry) season, after prolonged periods of high temperature, deeper soils will dry and PC will form, thus recording warm season Δ_{47}Ts. Contrasting with Andean climate, the Asian monsoon system effects warm and wet summer seasons in Central China, including the NETP and Chinese Loess Plateau. This implies that formation of PC in these regions would require sufficient time for soil to dry under warm temperatures following major precipitation events. We presume this occurs in the late Summer and early Fall, coinciding with the time of the year where rainfall starts to decrease and soils at depth are warmest, based on our modeling (Supplemental Fig. 3).

As discussed above, formation of PC in the Plio-Pleistocene in the NETP is inferred to have occurred at depths shallower than 100 cm. Studies have shown that PC formed at depths shallower than 30–40 cm does not record seasonal temperatures of carbonate formation (Burgener et al., 2016; Quade et al., 2013). This indicates that PC in this study that would actually record seasonal temperatures of carbonate formation would have to have formed at depths ranging from 40 to 100 cm. In this study, we assume that they did form between these depths. Because it is not possible to determine the actual depths of PC formation of our samples, we chose a depth of 50 cm as a representative depth to Bk horizon. Based on the NETP soil temperature model explained in section 2.5.2., I have calculated model temperatures for each station during the JJA period for depths ranging from 40 to 100 cm. Supplemental Figure 9 shows a plot of MAAT versus soil JJA temperatures at depths ranging from 40 to 100 cm and shows the difference between its linear regression line and the linear regression line for soil depths of 50 cm. The latter was used in this study's calculations of paleotemperature and paleoelevation in the Lake Qinghai Basin, as explained in the Methods section (2.4.5). Because there is more variability in the temperatures modeled to represent depths ranging 40–100 cm than in temperatures at depth 50 cm, the uncertainties in paleotemperature and paleoelevation would be larger if we used the relationships between MAATs and soil temperatures (40–100 cm) in the Monte Carlo Simulations for each sample presented in Supplemental Tables 9–12.

SUPPLEMENTAL REFERENCES CITED

Breecker, D.O., Sharp, Z.D., and McFadden, L.D., 2009, Seasonal bias in the formation and stable isotopic composition of pedogenic carbonate in modern soils from central New Mexico, USA: Bulletin of the Geological Society of America, v. 121, p. 630–640, https://doi.org/10.1130/B26413.1.

Burgener, L., Huntington, K.W., Hoke, G.D., Schauer, A., Ringham, M.C., Latorre, C., and Díaz, F.P., 2016, Variations in soil carbonate formation and seasonal bias over >4 km of relief in the western Andes (30°S) revealed by clumped isotope thermometry: Earth and Planetary Science Letters, v. 441, p. 188–199, https://doi.org/10.1016/j.epsl.2016.02.033.

Chen, J., Wyrwoll, K. H., Lu, Y., Krapez, B., Wan, J., and Liu, J. , 2006, Magnetochronology of the Yumen Conglomerates and Multi-Pulsed Folding and Thrusting in the Northern Qilian Shan: Quaternary Sciences, v. 26, p. 20–31 (in Chinese). doi:10.3321/j.issn:1001-7410.2006.01.004

Davis, J.C., 2002. Statistics and Data Analysis in Geology. John Wiley & Sons, New York, 638 pp.

Fang, X., Garzione, C., Van der Voo, R., Li, J., and Fan, M., 2003, Flexural subsidence by 29 Ma on the NE edge of Tibet from the magnetostratigraphy of Linxia Basin, China: Earth and Planetary Science Letters, v. 210, p. 545–560, doi:10.1016/S0012-821X(03)00142-0.
Fang, X., Zhao, Z., Li, J., Yan, M., Pan, B., Song, C., and Dai, S., 2005, Magnetostratigraphy of the late Cenozoic Laojunmiao anticline in the northern Qilian Mountains and its implications for the northern Tibetan Plateau uplift: Science in China. Series D, Earth Sciences, v. 48, p. 1040–1051, https://doi.org/10.1360/03yd0188.
Fang, X., Zhang, W., Meng, Q., Gao, J., Wang, X., King, J., Song, C., Dai, S., and Miao, Y., 2007, High-resolution magnetostratigraphy of the Neogene Huaitoutala section in the eastern Qaidam Basin on the NE Tibetan Plateau, Qinghai Province, China and its implication on tectonic uplift of the NE Tibetan Plateau: Earth and Planetary Science Letters, v. 258, p. 293–306, https://doi.org/10.1016/j.epsl.2007.03.042.
Gregory, K.M., and McIntosh, W.C., 1996, Paleoclimate and paleoelevation of the Oligocene Pitch-Pinnacle flora, Sawatch Range, Colorado: Geological Society of America Bulletin, v. 108, p. 545–561, https://doi.org/10.1130/0016-7606(1996)108<0545:PAPOTO>2.3.CO;2.
Guo, Z.T., Ruddiman, W.F., Hao, Q.Z., Wu, H.B., Qiao, Y.S., Zhu, R.X., Peng, S.Z., Wel, J.J., Yuan, B.Y., and Llu, T.S., 2002, Onset of Asian desertification by 22 Myr ago inferred from loess deposits in China: Nature, v. 416, p. 159–163, https://doi.org/10.1038/416159a.
Hillel, D., 1982, Introduction to Environmental Soil Physics: New York, Academic. Press Inc..
Hu, X., Chen, D., Pan, B., Chen, J., Zhang, J., Chang, J., Gong, C., and Zhao, Q., 2019, Sedimentary evolution of the foreland basin in the NE Tibetan Plateau and the growth of the Qilian Shan since 7 Ma: Bulletin of the Geological Society of America, v. 131, p. 1744–1760, https://doi.org/10.1130/B35106.1.
Huntington, K.W., Wernicke, B.P., and Eiler, J.M., 2010, Influence of climate change and uplift on Colorado Plateau paleotemperatures from carbonate clumped isotope thermometry: Tectonics, v. 29, p. 1–19, https://doi.org/10.1029/2009TC002449.
Li, J., Fang, X., Song, C., Pan, B., Ma, Y., and Yan, M., 2014, Late Miocene – Quaternary rapid stepwise uplift of the NE Tibetan Plateau and its effects on climatic and environmental changes: Quaternary Research, v. 81, p. 400–423, https://doi.org/10.1016/j.yqres.2014.01.002.
Li, J.J., et al., 1996, Late Cenozoic magnetostratigraphy (11 - 0 Ma) of the Dongshanding and Wangjiashan sections in the Longzhong Basin, western China: Netherlands Journal of Geosciences, v. 76, p. 121–134, https://doi.org/10.1023/A:1003153717799.
Liu, X.W., 2017, Characteristics of active tectonics and the deformation pattern of the Jiuxi Basin at the western Qilian Shan [Ph.D. thesis]: Lanzhou, China , Lanzhou University, 111 p. (in Chinese).
Liu, X., Yu, Z., Dong, H., and Chen, H.F., 2014, A less or more dusty future in the Northern Qinghai-Tibetan Plateau?: Scientific Reports, v. 4, p. 1–6, https://doi.org/10.1038/srep06672.
Meyer, H.W., 1986, An evaluation of the methods for estimating paleoaltitudes using Tertiary floras from the Rio Grande rift vicinity: New Mexico and Colorado: , Berkeley University of California.
Meyer, H.W., 1992, Lapse rates and other variables applied to estimating paleoaltitudes from fossil floras: Palaeogeography, Palaeoclimatology, Palaeoecology, v. 99, p. 71–99, https://doi.org/10.1016/0031-0182(92)90008-S.

Moore, J.J., Hughen, K.A., Miller, G.H., and Overpeck, J.T., 2001, Little Ice Age recorded in summer temperature reconstruction from varved sediments of Donard Lake, Baffin Island, Canada: Journal of Paleolimnology, v. 25, p. 503–517, https://doi.org/10.1023/A:1011181301514.

Palumbo, L., Hetzel, R., Tao, M., Li, X., and Guo, J., 2009, Deciphering the rate of mountain growth during topographic presteady state: An example from the NE margin of the Tibetan Plateau: Tectonics, v. 28, https://doi.org/10.1029/2009TC002455.

Quade, J., Eiler, J., Daëron, M., and Achyuthan, H., 2013, The clumped isotope geothermometer in soil and paleosol carbonate: Geochimica et Cosmochimica Acta, v. 105, p. 92–107, https://doi.org/10.1016/j.gca.2012.11.031.

Schneider, T., 2007, Thermal stratification of the extratropical troposphere, *in* Schneider, T., and Sobel, A.H., eds., The Global Circulation of the Atmosphere: Princeton, Princeton University Press, p. 47–77.

Sun, D., Zhang, Y., Han, F., Zhang, Y., Yi, Z., Li, Z., Wang, F., Wu, S., and Li, B., 2011, Magnetostratigraphy and palaeoenvironmental records for a Late Cenozoic sedimentary sequence from Lanzhou, Northeastern margin of the Tibetan Plateau: Global and Planetary Change, v. 76, p. 106–116, https://doi.org/10.1016/j.gloplacha.2010.12.006.

Wang, W., Zhang, P., Pang, J., Garzione, C., Zhang, H., Liu, C., Zheng, D., Zheng, W., and Yu, J., 2016, The Cenozoic growth of the Qilian Shan in the northeastern Tibetan Plateau: A sedimentary archive from the Juxi Basin: Journal of Geophysical Research: Solid Earth, v. 121, p. 2235–2257, doi:10.1002/2015JB012689.

Wang, H., Lu, H., Zhao, L., Zhang, H., Lei, F., and Wang, Y., 2019, Asian monsoon rainfall variation during the Pliocene forced by global temperature change: Nature Communications, v. 10, p. 4–11, https://doi.org/10.1038/s41467-019-13338-4.

Williams, P.J., and Smith, M.W., 1989, The Frozen Earth: Fundamentals of Geocryology, Stud. Polar Res.: New York, Cambridge University Press, https://doi.org/10.1017/CBO9780511564437.

Yan, M., Fang, X., Van Der Voo, R., Song, C., and Li, J., 2013, Neogene rotations in the Jiuquan Basin, Hexi Corridor, China, *in* Jovane, L., Herrero-Bervera, E., Hinnov, L.A. and Housen, B.A., eds., Magnetic Methods and the Timing of Geological Processes: Geological Society, London, Special Publications,v. 373, p. 173–189. https://doi.org/10.1144/SP373.6

Yang, B., Qin, C., Wang, J., He, M., Melvin, T.M., Osborn, T.J., and Briffa, K.R., 2014, A 3,500-year tree-ring record of annual precipitation on the northeastern Tibetan Plateau: Proceedings of the National Academy of Sciences of the United States of America, v. 111, p. 2903–2908, https://doi.org/10.1073/pnas.1319238111.

Zamanian, K., Pustovoytov, K., and Kuzyakov, Y., 2016, Pedogenic carbonates: Forms and formation processes: Earth-Science Reviews, v. 157, p. 1–17, https://doi.org/10.1016/j.earscirev.2016.03.003.

Zhang, H.P., Craddock, W.H., Lease, R.O., Wang, W.T., Yuan, D.Y., Zhang, P.Z., Molnar, P., Zheng, D.W., and Zheng, W.J., 2012, Magnetostratigraphy of the Neogene Chaka basin and its implications for mountain building processes in the north-eastern Tibetan Plateau: Basin Research, v. 24, p. 31–50, https://doi.org/10.1111/j.1365-2117.2011.00512.x.

Zhang, W., Fang, X., Song, C., Appel, E., Yan, M., and Wang, Y., 2013, Late Neogene magnetostratigraphy in the western Qaidam Basin (NE Tibetan Plateau) and its constraints on active tectonic uplift and progressive evolution of growth strata: Tectonophysics, v. 599, p. 107–116, https://doi.org/10.1016/j.tecto.2013.04.010.

Zhao, Z., Fang, X., and Li, J., 2001, Late Cenozoic magnetic polarity stratigraphy in the Jiudong Basin, northern Qilian Mountain: Science in China. Series D, Earth Sciences, v. 44, p. 243–250, https://doi.org/10.1007/BF02911993.

Zheng, D., Wang, W., Wan, J., Yuan, D., Liu, C., Zheng, W., Zhang, H., and Pang, J., 2017, Progressive northward growth of the northern Qilian Shan – Hexi Corridor (northeastern Tibet) during the Cenozoic: Lithosphere, v. 9, no. 3, p. 408–416, https://doi.org/10.1130/L587.1.

Richter, F., Garzione, C.N., Liu, W., Qiang, X., Chang, H., Cheng, F., Li, X., Tripati, A., 2021, Plio-Pleistocene cooling of the northeastern Tibetan Plateau due to superimposed global cooling and surface uplift: GSA Bulletin.

SUPPLEMENTARY FIGURES

Supplementary Figure 1. Division of the core.

Supplementary Figure 2. Core pictures showing the locations from where clumped-isotope samples were collected.

Supplementary Figure 3. Annual soil temperature variation and soil-temperature profiles in the literature compared to our models.

Supplementary Figure 4. Relationship between air and ground temperatures

Supplementary Figure 5. Changes in modern T-elevation gradients according to variations in mean temperatures.

Supplementary Figure 6. Plots of Δ47 vs. 18O ‰ and 13C ‰ vs. 18O ‰ from clumped-isotope analyses.

Supplementary Figure 7. Plio-Pleistocene MAATs and paleoelevation estimates for the Lake Qinghai Basin (LQB) compared to regional and global records (AMJJASO transfer functions).

Supplementary Figure 8. Plio-Pleistocene MAATs and paleoelevation estimates for the Lake Qinghai Basin (LQB) compared to regional and global records (JJA transfer functions).

Supplementary Figure 9. Modeled (underground) soil temperatures at depths ranging from 40-100 cm. See Supplementary Note 3 for details.

Supplementary Figure 10. Results of tests of significance between mean MAATs in the 4 age groups. The figure shows two-sample z-tets and two-sample-one-tail t-tests to help decided whether there is significant difference between the mean MAAT values of groups 1 and 2, 2 and 3, 3 and 4.

Supplementary Figure 11. Results of tests of significance between mean MAATs in the oldest segment (groups 1 and 2) and mean MAATs in the youngest segment (groups 3 and 4) (i.e., before and after 3.6 Ma). The figure shows two-sample z-tests and two-sample-one-tail t-tests to help decide whether there is a significant difference in mean MAATs of groups 1+2 (4.85 to 3.7 Ma) and groups 3+4 (3.5 to 2.06 Ma).

Supplementary Figure 12. Mineral compositions of 20 samples from the Yilang core spanning 3.0 to 3.8 Ma and sand percentage spanning 2.0-5.1 Ma. a) Composition of all samples. b) Percentage of calcite, dolomite and quartz. c) Percentage of calcite and dolomite. All samples that have been excluded from T calculations have a percentage of dolomite higher than 1%. d) 100% stacked bar plot showing the proportion of calcite, dolomite and quartz. e) 100% stacked bar plot showing the relative proportions of carbonatic minerals calcite and dolomite. f) Grain-size larger than sand, SEM samples, and clumped isotope samples from 2.0 to 5.1 Ma.

Supplementary Figures

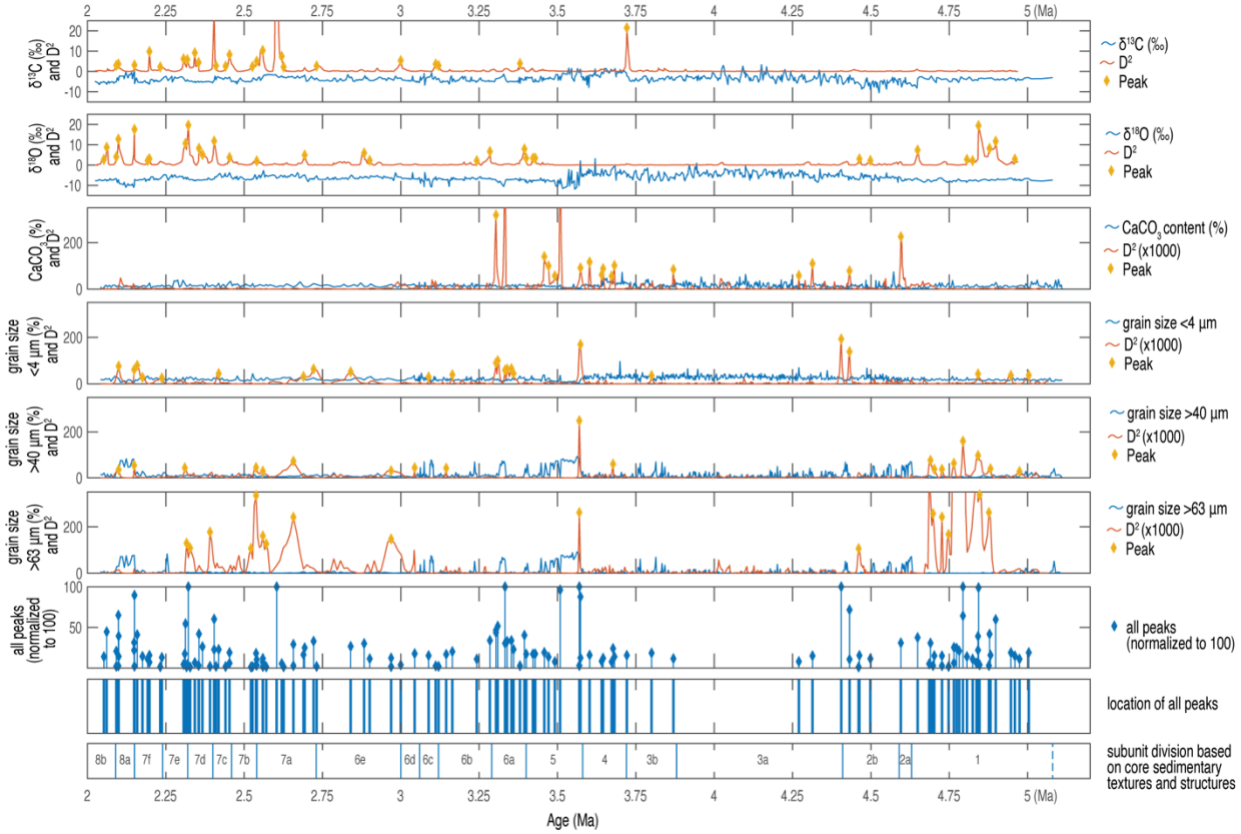

Supplementary Figure 1. Division of the core. The upper 6 diagrams show $\delta^{18}O$ ‰, $\delta^{13}C$ ‰, grain size <4 µm %, grain size >40 µm %, grain size >63 µm % and $CaCO_3$ content % values and respective calculated D^2 values. Peaks at each D^2 plot indicate higher rates of change in the dependent variable. We normalized and combined peaks obtained from all variables to identify significant and/or coincident changes in grain size and stable isotope compositions. We plotted location of peaks vs. time to define boundaries and compared their location to the boundaries we set based on the core sedimentary features (see Methods).

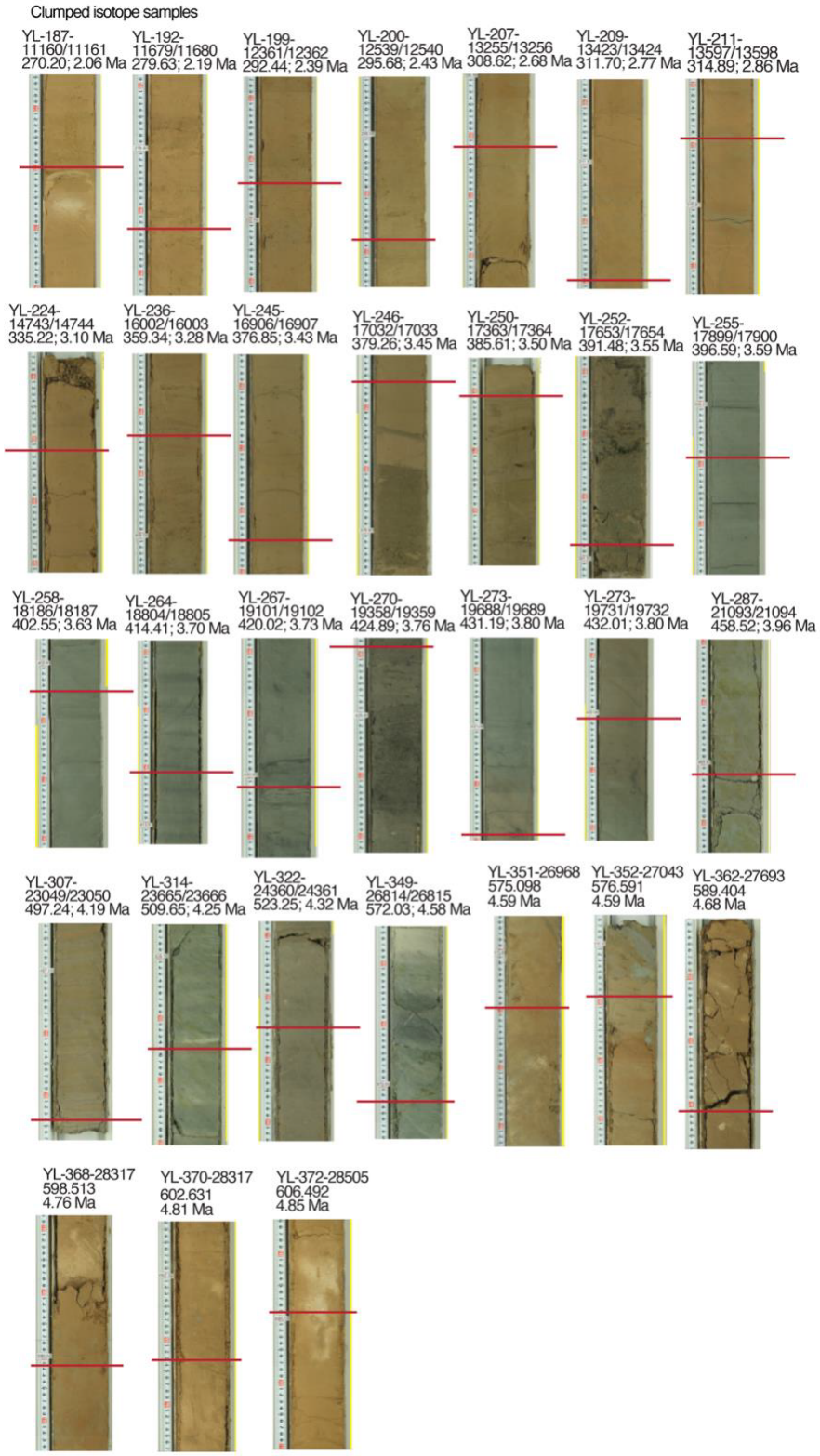

Supplementary Figure 2. Core pictures showing the locations from where clumped-isotope samples were collected.

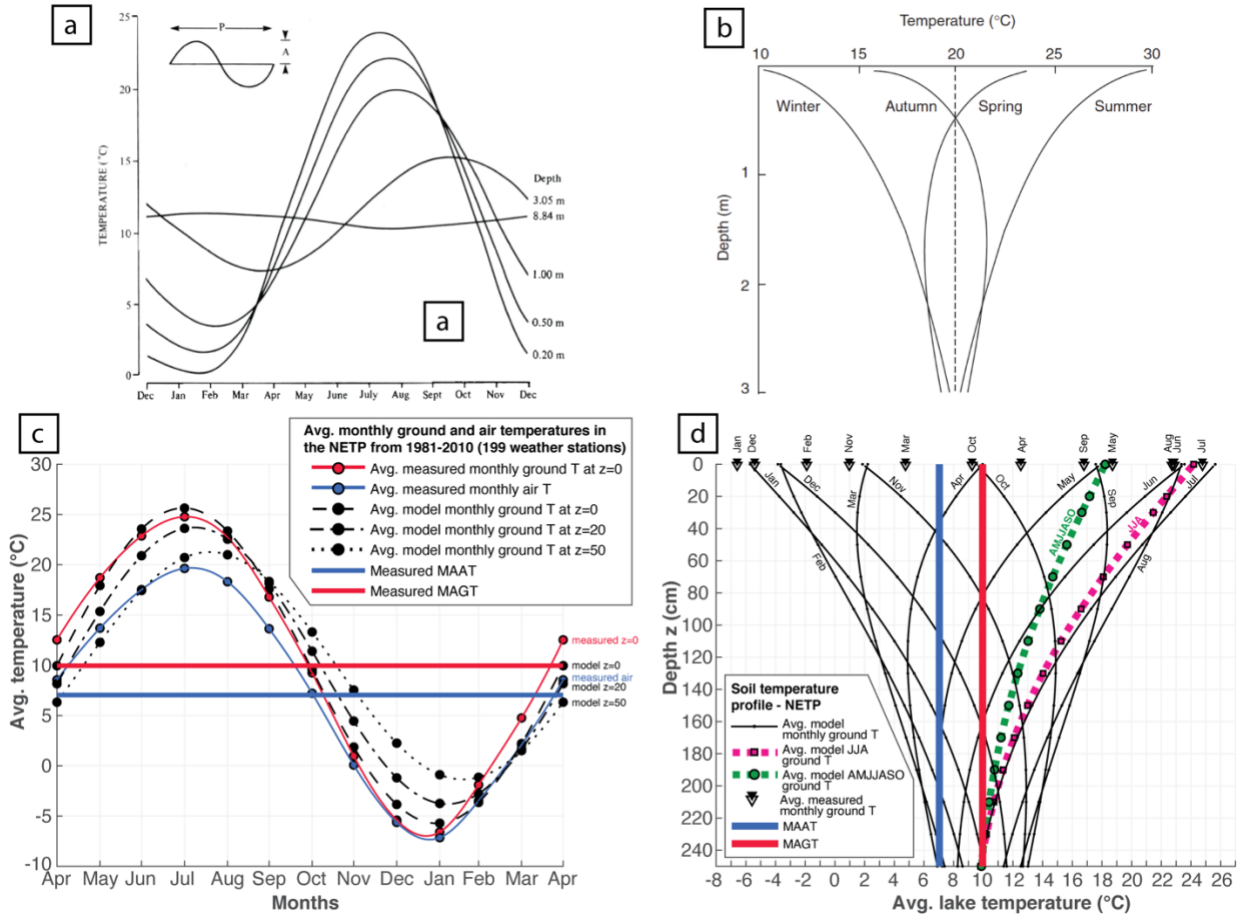

Supplementary Figure 3. Annual soil temperature variation and soil-temperature profiles in the literature compared to our models. (a) Annual temperature variation in unfrozen soil (reproduced from Williams and Smith, 1989, after Carson and Moses, 1963). (b) Soil-temperature profile as it varies from season to season in a frost-free region (reproduced from Hilel, 1982). (c) Model and measured temperatures in the NETP over the year based on data from 199 weather stations in the NETP region (this study). At z=0, measured avg. ground surface Ts and model avg. ground surface Ts closely agree, particularly on the warmest half of the year. (d) Modeled soil temperature profile in the NETP as it varies monthly, during the JJA period and during the AMJJASO period (this study). Both (c) and (d) represent average values obtained from all weather stations.

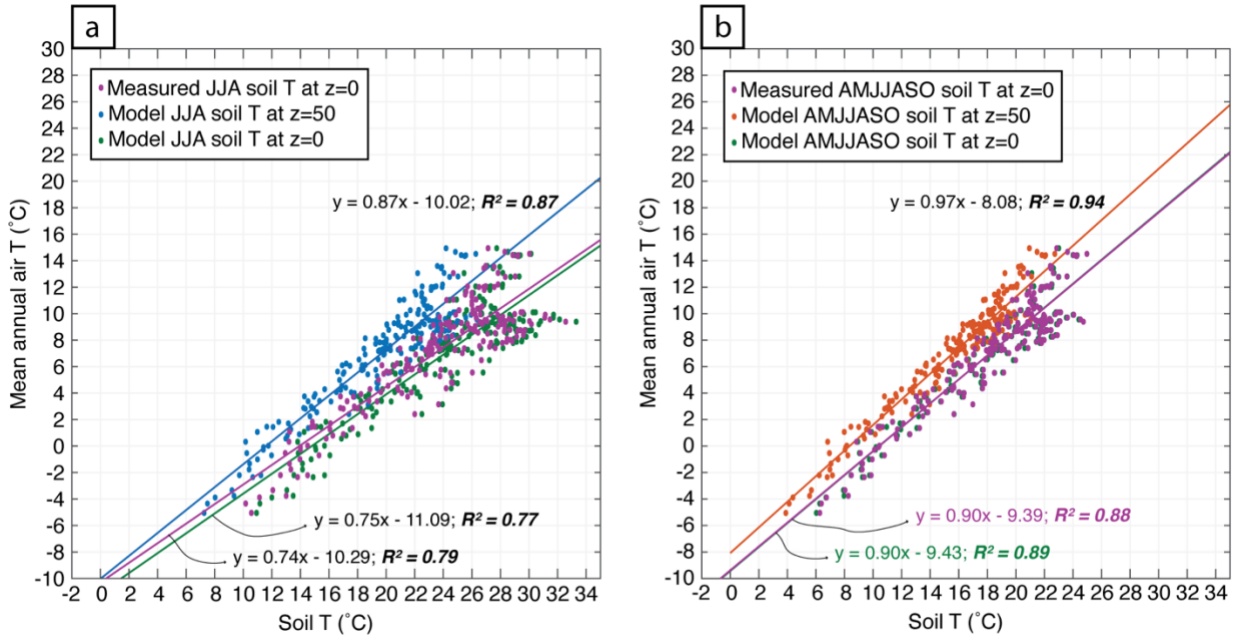

Supplementary Figure 4. Relationship between air and ground temperatures. Figures show depths (z) of z=0 (measured and modeled) and z=50 (modeled) during (a) JJA and (b) AMJJASO periods (n=199).

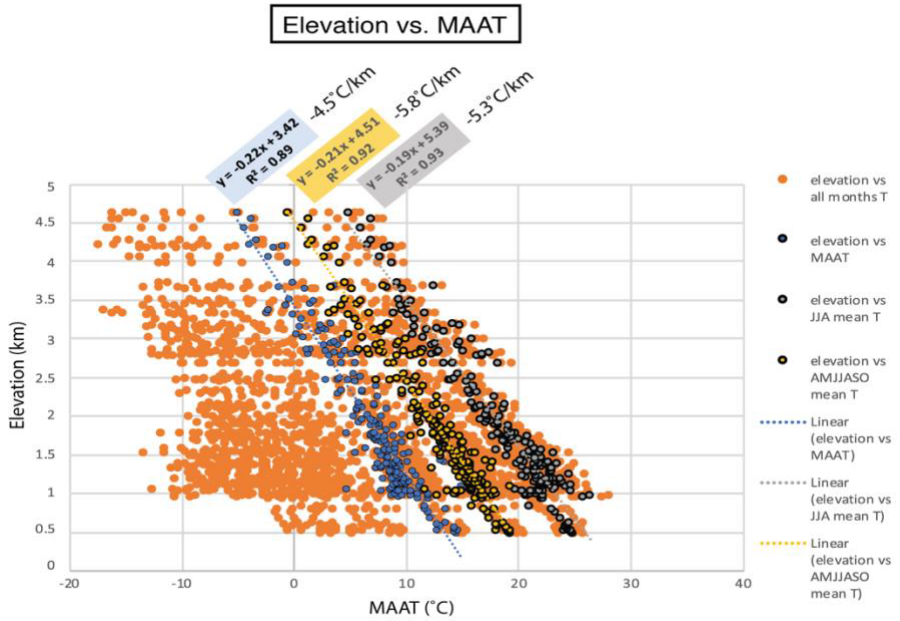

Supplementary Figure 5. Changes in modern T-elevation gradients according to variations in mean temperatures.

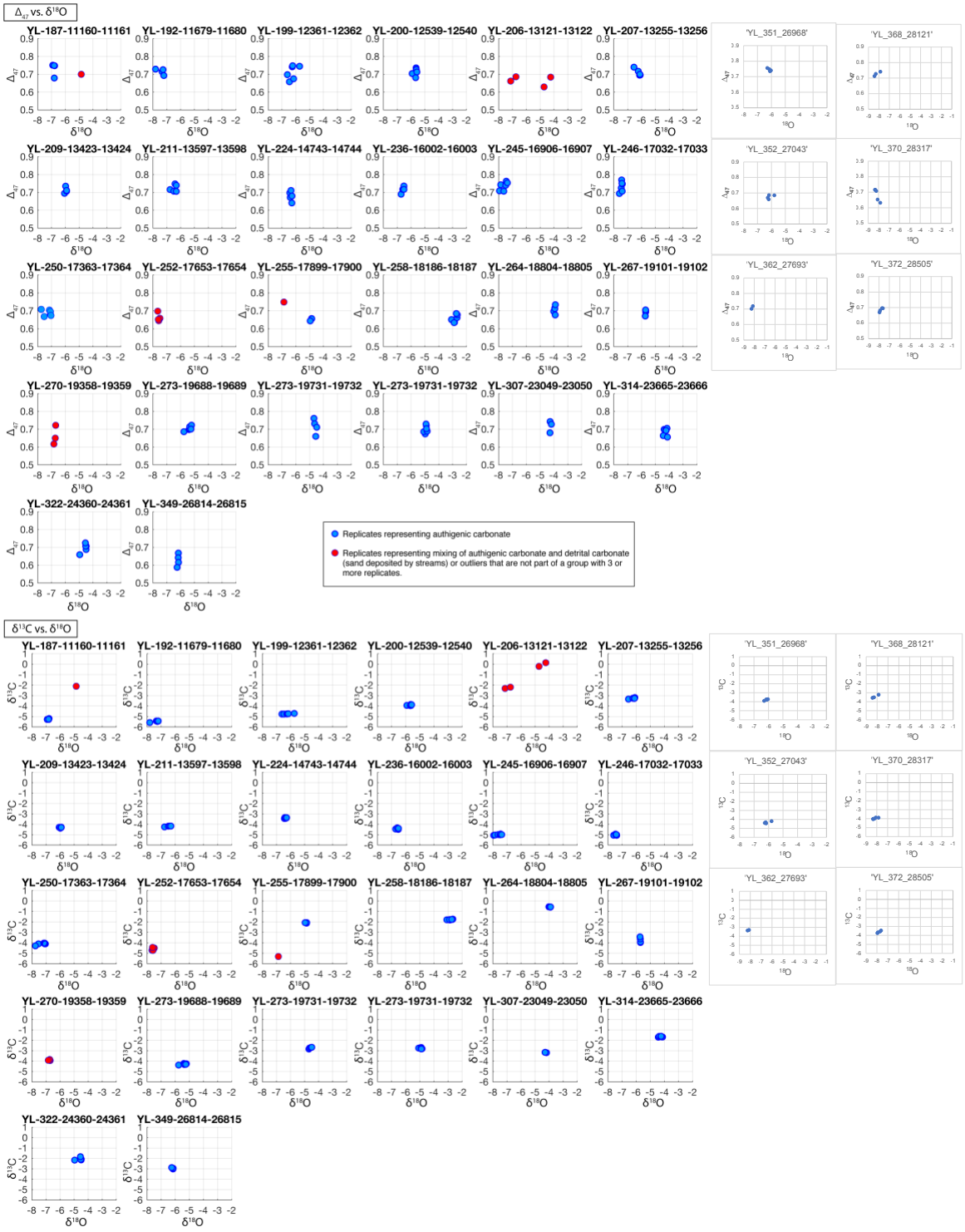

Supplementary Figure 6. Plots of Δ_{47} vs. $\delta^{18}O$ ‰ and $\delta^{13}C$ ‰ vs. $\delta^{18}O$ ‰ from clumped-isotope analyses. Replicates shown as red dots and sample YL-206 (2.6 Ma) was excluded from the dataset discussed in this study because of its clear bimodal distribution and coarse grain-size. Samples YL-252 (3.55 Ma) and YL-270 (3.75 Ma) are shown in Fig. 5d as gray dots. They were, however, excluded from calculations of MAATs because of they also showed a bimodal distribution and were collected from intervals with a coarse grain-size, so we were not confident in the meaning of their signal. We interpret these samples may represent some degree of mixing of authigenic carbonate and detrital carbonate and/or incomplete carbonate digestion during analysis.

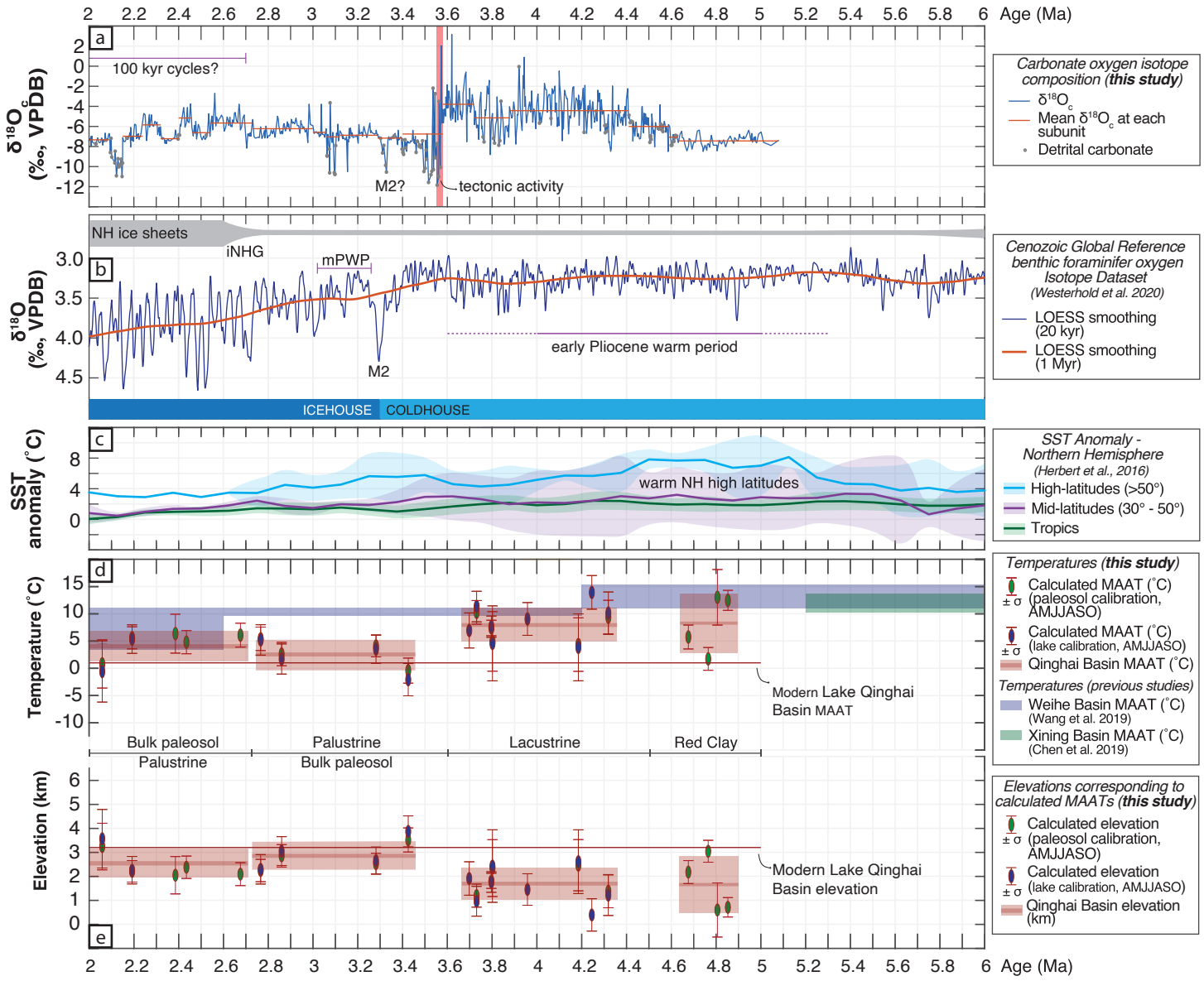

Supplementary figure 7

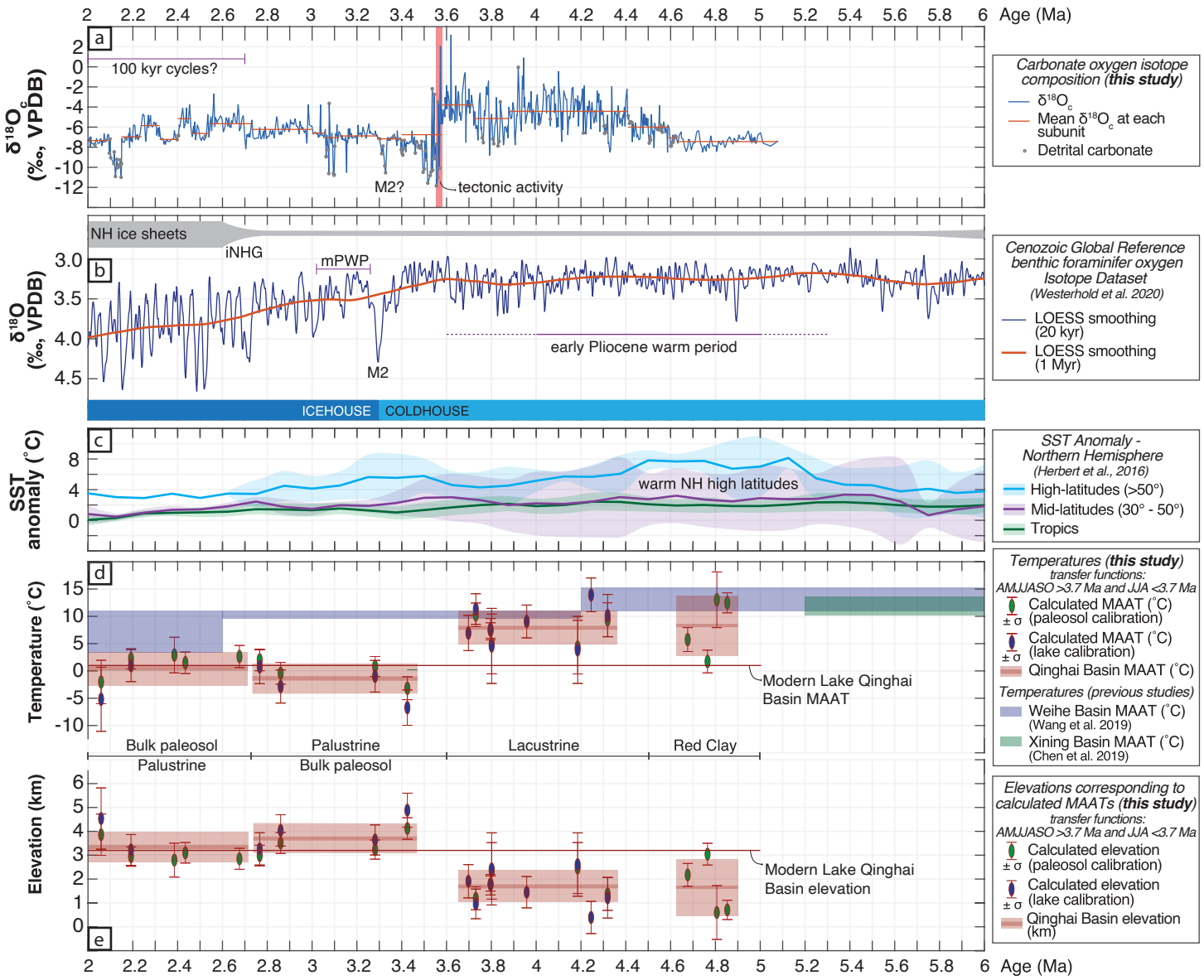

Supplementary figure 8

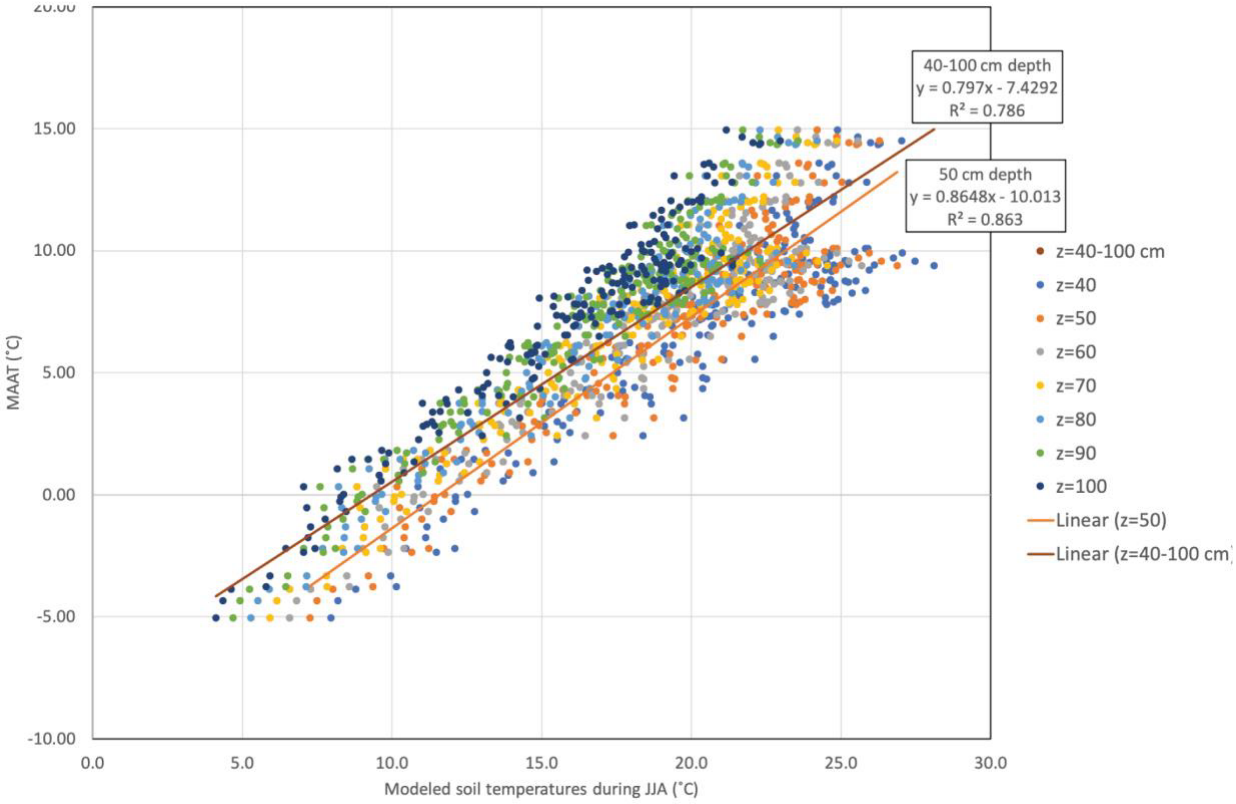

Supplementary Figure 9. Modeled (underground) soil temperatures at depths ranging from 40-100 cm. See Supplementary Note 3 for details.

Here we show two-sample z-tests and two-sample-one-tail t-tests to decide whether there is a significant difference between the mean values of groups 4 and 3; 3 and 2; 2 and 1.

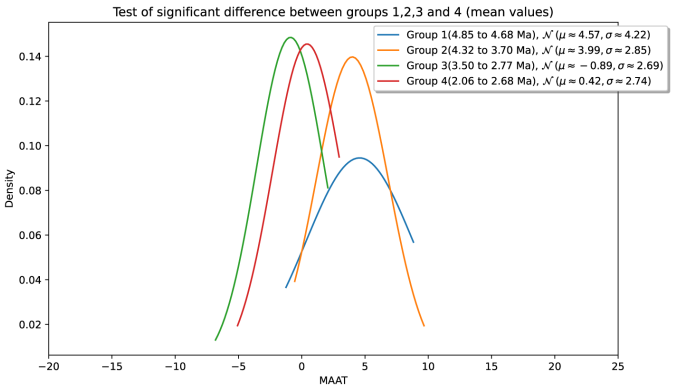

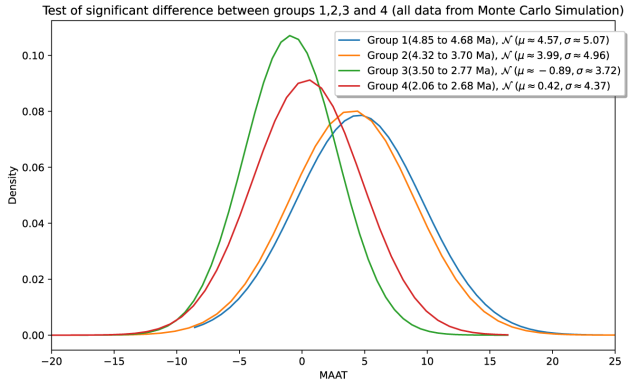

H0: Null hypothesis
Ha: Alternative hypothesis

Hypothesis Testing - Groups 2 and 3

Hypothesis Test: H0: μ(2) = μ(3); Ha: μ(2) ≠ μ(3)
Z-test: z-test value for the sample means of groups 2 and 3 is 3.7
Z-test: p-value for the sample means of groups 2 and 3 is 0.0
Conclusion: Since p-value(=0.000213) > alpha(=0.05), We do not reject the null hypothesis H0. So we conclude that the difference between μ(2) and μ(3) is statistically significant, and probably μ(2) ≠ μ(3).

Hypothesis Test: H0: μ(2) = μ(3); Ha: μ(2) > μ(3)
T-test: Test statistic is 3.702857
T-test: p-value for one tailed t-test is 0.000755
Conclusion: Since p-value(=0.000755) < alpha(=0.05), We reject the null hypothesis H0. So we conclude that the difference between μ(2) and μ(3) is statistically significant, and probably μ(2) ≠ μ(3).

Hypothesis Testing - Groups 1 and 2

Hypothesis Test: H0: μ(1) = μ(2); Ha: μ(1) ≠ μ(2)
Z-test: z-test value for the sample means of groups 1 and 2 is 0.29
Z-test: p-value for the sample means of groups 1 and 2 is 0.77
Conclusion: Since p-value(=0.769068) > alpha(=0.05), We do not reject the null hypothesis H0. So we conclude that the difference between μ(1) and μ(2) is not statistically significant, and probably μ(1) = μ(2).

Hypothesis Testing: H0: μ(1) = μ(2); Ha: μ(1) > μ(2)
T-test: Test statistic is 0.293594
T-test: p-value for one tailed t-test is 0.386546
Conclusion: Since p-value(=0.386546) > alpha(=0.05), We do not reject the null hypothesis H0. So we conclude that the difference between μ(1) and μ(2) is not statistically significant, and probably μ(1) = μ(2).

Hypothesis Testing - Groups 3 and 4

Hypothesis Test: H0: μ(3) = μ(4); Ha: μ(3) ≠ μ(4)
Z-test: z-test value for the sample means of groups 3 and 4 is -0.87
Z-test: p-value for the sample means of groups 3 and 4 is 0.38
Conclusion: Since p-value(=0.383788) > alpha(=0.05), We do not reject the null hypothesis H0. So we conclude that the difference between μ(3) and μ(4) is not statistically significant, and probably μ(3) = μ(4).

Hypothesis Testing: H0: μ(3) = μ(4); Ha: μ(3) > μ(4)
T-test: Test statistic is -0.870937
T-test: p-value for one tailed t-test is 0.800207
Conclusion: Since p-value(=0.800207) > alpha(=0.05), We do not reject the null hypothesis H0. So we conclude that the difference between μ(3) and μ(4) is not statistically significant, and probably μ(3) = μ(4).

Supplementary Figure 10. Results of tests of significance between mean MAATs in the 4 age groups. The figure shows two-sample z-tets and two-sample-one-tail t-tests to help decided whether there is significant difference between the mean MAAT values of groups 1 and 2, 2 and 3, 3 and 4.

Here we show two-sample z-tests and two-sample-one-tail t-tests to decide whether there is a significant difference between the mean values of groups 1+2 (4.85 to 3.7 Ma) and 3+4 (3.5 to 2.06 Ma).

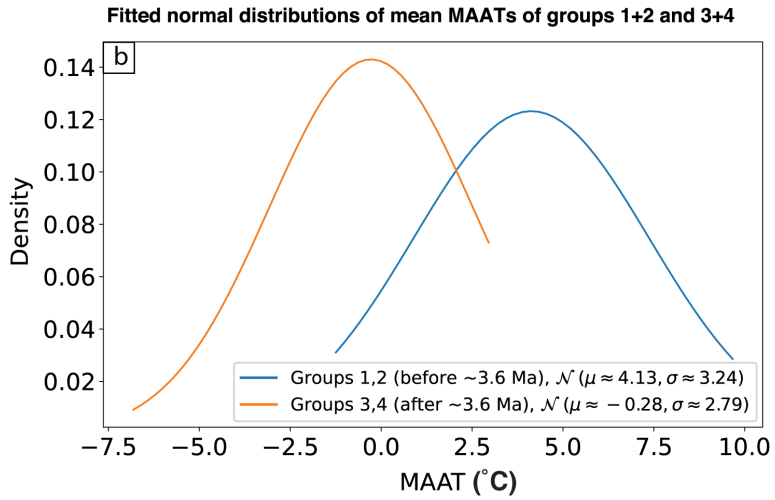

H0: Null hypothesis
Ha: Alternative hypothesis

Hypothesis Testing - Groups 1+2 and 3+4

Hypothesis Test: H0: μ(3+4) = μ(1+2); Ha: μ(3+4) ≠ μ(1+2)
Z-test: z-test value for the sample means of groups 1+2 and 3+4 is -3.9671
Z-test: p-value for the sample means of groups 1+2 and 3+4 is 0.0001
Conclusion: Since p-value(=0.000073) < alpha(=0.05), We reject the null hypothesis H0. So we conclude that the difference between μ(3+4) and μ(1+2) is statistically significant, and probably μ(3+4) ≠ μ(1+2).

Hypothesis Test: H0: μ(3+4) = μ(1+2); Ha: μ(3+4) ≠ μ(1+2)
Z-test: z-test value for all the data (Monte Carlo Simulation, n=10000 for each sample) in groups 1+2 and 3+4 is 0.0
Z-test: p-value for all the data (Monte Carlo Simulation, n=10000 for each sample) in groups 1+2 and 3+4 is 0.0
Conclusion: Since p-value(=0.000000) < alpha(=0.05), We reject the null hypothesis H0. So we conclude that the difference between μ(3+4)(all simulated data) and μ(1+2)(all simulated data) is statistically significant, and probably μ(3+4) ≠ μ(1+2).

Hypothesis Test: H0: μ(3+4) = μ(1+2); Ha: μ(3+4) > μ(1+2)
T-test: Test statistic is 3.967107
T-test: p-value for one tailed t-test is 0.000209
Conclusion: Since p-value(=0.000209) < alpha(=0.05), We reject the null hypothesis H0. So we conclude that the difference between μ(3+4) and μ(1+2) is statistically significant, and probably μ(3+4) ≠ μ(1+2).

Supplementary Figure 11. Results of tests of significance between mean MAATs in the oldest segment (groups 1 and 2) and mean MAATs in the youngest segment (groups 3 and 4) (i.e., before and after 3.6 Ma). The figure shows two-sample z-tests and two-sample-one-tail t-tests to help decide whether there is a significant difference in mean MAATs of groups 1+2 (4.85 to 3.7 Ma) and groups 3+4 (3.5 to 2.06 Ma).

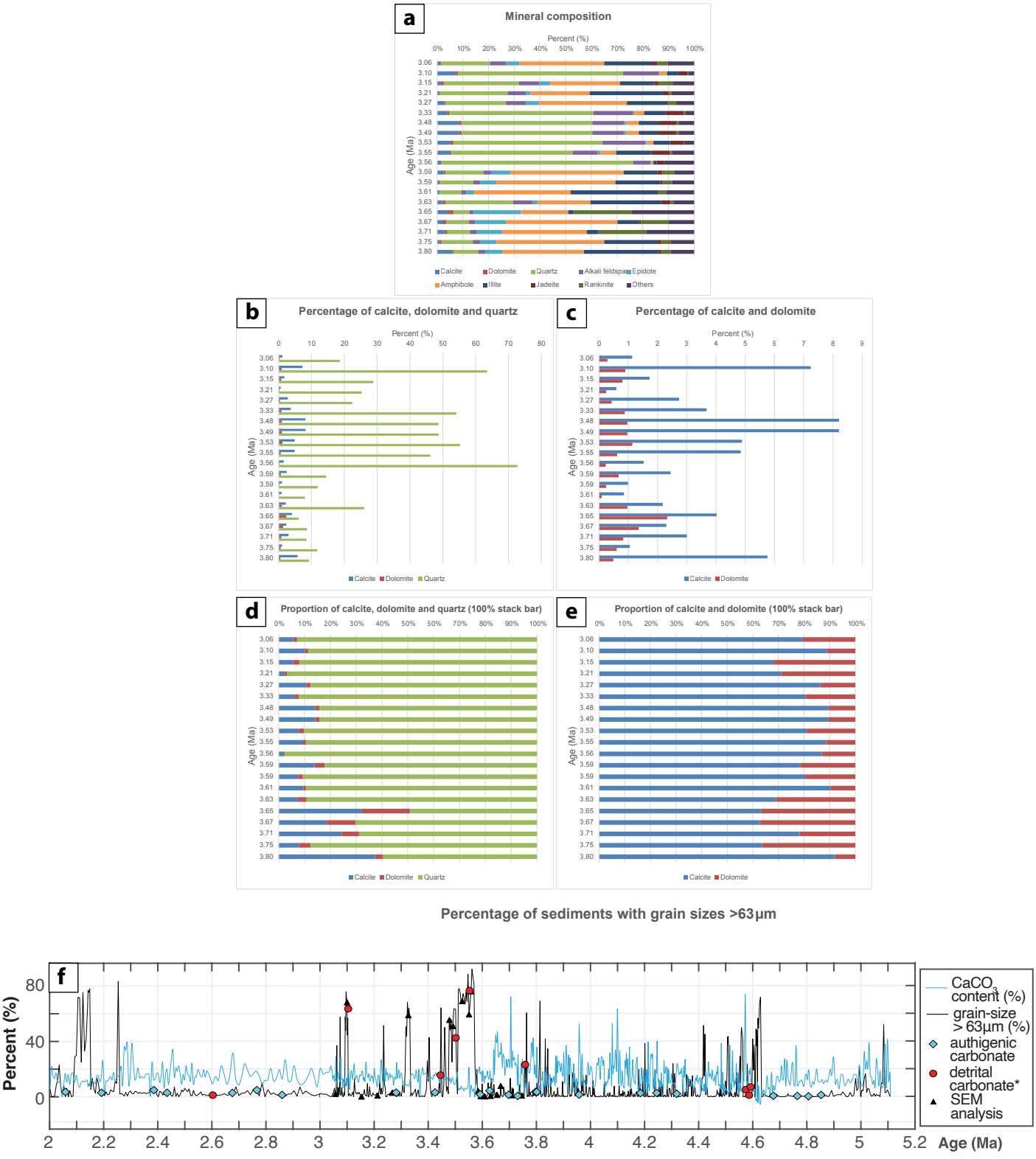

Supplementary Figure 12